Effects of Ni and Co on Phase Transformation and Shape Memory Effect of Ti–Pd–Zr Alloys

Yoko Yamabe-Mitarai[1,2] · Brandon Ohl[3] · Karolina Bogdanowicz[4] ·
Ewelina Muszalska[4]

Abstract Effect of single and simultaneous addition of Ni and Co to $Ti_{45}Zr_5Pd_x$ on the phase transformation and strain recovery of the alloys was investigated to understand multi-component effect on high-temperature shape memory alloys. The martensitic transformation from B2 to B19 structures occurred in $Ti_{45}Zr_5Pd_{40}Ni_{10}$, $Ti_{45}Zr_5Pd_{40}Co_{10}$, $Ti_{45}Zr_5Pd_{40}Ni_8Co_2$, and $Ti_{45}Zr_5Pd_{40}Ni_2Co_8$. In contrast, at room temperature, martensitic transformation did not occur and the B2 structure was stable in $Ti_{45}Zr_5Pd_{30}Ni_{20}$ and $Ti_{45}Zr_5Pd_{40}Ni_5Co_5$. This is due to the effect of Ni for $Ti_{45}Zr_5Pd_{30}Ni_{20}$ and the effect of multi-component for $Ti_{45}Zr_5Pd_{40}Ni_5Co_5$. The shape memory effect was investigated using a thermal cyclic test. The perfect shape recovery was obtained after the repeated thermal cyclic test, indicating the potential of TiZrPd (Ni, Co) alloys as shape memory alloys.

✉ Yoko Yamabe-Mitarai
  mitarai.yoko@edu.k.u-tokyo.ac.jp

1 National Institute for Materials Science (NIMS), 1-2-1 Sengen, Tsukuba, Ibaraki 305-0047, Japan

2 Graduate School of Frontier Sciences, The University of Tokyo, 5-1-5 Kashiwanoha, Kashiwa, Chiba 277-8568, Japan

3 Northwestern University, 633 Clark St, Evanston, IL 60208, USA

4 Warsaw University of Technology, pl Politechniki 1, 00-661 Warsaw, Poland

Introduction

The shape memory effect (SME) occurs by reverse martensitic transformation (MT). TiNi is the most commonly used shape memory alloy (SMA), but the martensitic transformation temperature (MTT) of TiNi from the B2 to B19 structures is lower than 100 °C. To expand the applications of SMAs, the MTTs should be increased to raise the operation temperatures of SMAs [1]. Thus, various techniques have been employed to raise the MTT of TiNi, such as the addition of alloying elements such as Pt, Pd, Hf, and Zr into TiNi.

Recently, Hf-added TiNi alloys have attracted attention due to their high strength by nanoprecipitates and low cost; however, their MTTs are between 100 and 200 °C [2–10]. The most attractive high-temperature shape memory alloy composition is $Ni_{50.3}Ti_{29.7}Hf_{20}$, and the perfect shape recovery was obtained even under 500–700 MPa with a large work output, ~ 20 J/cm^3, equivalent to that of TiNi. In addition, Hf raised the MTTs of TiNi alloys, and the highest martensite start temperature (M_s) was found as ~ 500 °C for $Ni_{49.8}Ti_{20.2}Hf_{30}$ [10], indicating the potential of TiNi-Hf alloys with nanoprecipitates as high-temperature shape memory alloys (HT-SMAs).

High-entropy alloys (HEAs) have attracted attention for HT-SMA applications [11–14]. HEAs are multi-component equiatomic or near-equiatomic alloys and are expected to function as the next-generation structural materials. HEAs are also expected as high-temperature materials since they have severe lattice distortion and sluggish diffusion. For

example, $Ti_{16.667}Zr_{16.667}Hf_{16.667}Ni_{25}Cu_{25}$ [11] was the first attempt of HEAs as SMAs. It was found that $Ti_{16.667}Zr_{16.667}Hf_{16.667}Ni_{25}Cu_{25}$, as well as TiNi, had the MT from B2 to B19, and the austenite finish temperature (A_f) was 337 °C, and the martensite finish temperature (M_f) was 127 °C. The complete recovery was found between 127 and 377 °C, and the large strain recovery, approximately 4.9%, was obtained under 650 MPs due to the solid-solution hardening effect [12, 13]. The most impacted investigation was found in $Ni_{25}Pd_{25}Ti_{25}Hf_{25}$ and $Ni_{25}Pd_{25}Ti_{16.6}Hf_{16.6}Zr_{16.6}$ [14]. Their MTs from the B2 to B19 structure as well as TiPd occurred, and their A_f and A_s were approximately 700 and 780 °C, respectively, indicating HT-SMA characteristics [14].

We have focused on TiPd [15–18], TiAu [19, 20], and TiPt [21–29] as possible new HT-SMAs because MT occurs from B2 to B19 structure [30]. The MTTs of TiPd, TiAu, and TiPt are approximately 570, 600, and 1000 °C [31]. In addition to the understanding of the third element addition on the MT and the SME, we have investigated the multi-component alloys. Although their alloy compositions were not equiatomic, we considered that multi-component alloys have a similar HEA effect due to the increase in entropy compared with conventional alloys. Then, the MT and SME of the Ti–Pd–Pt–Zr quaternary alloys were investigated [32, 33]. The MTTs increased with the increase in Pt concentration, and the highest A_f was obtained at 935 °C in $Ti_{45}Pt_{45}Pd_5Zr_5$ [32]. However, the perfect strain recovery was not obtained in all the tested alloys [32, 33]. Then, multi-component alloys, TiZrPdPtNi, were investigated to understand the multi-component effect on MT and SME [34]. The two HEAs ($\Delta S_{mix} = 1.5R$), $Ti_{35}Zr_{15}Pd_{20}Ni_{15}Pt_{15}$ and $Ti_{40}Zr_{10}Pd_{20}Ni_{15}Pt_{15}$, and two medium entropy alloys (MEAs, $\Delta S_{mix} = 1.3R$), $Ti_{45}Zr_5Pd_{20}Ni_5Pt_{25}$ and $Ti_{45}Zr_5Pd_{20}Ni_{10}Pt_{20}$, were investigated. Here ΔS_{mix} is the mixing entropy defined by Eq. (1).

$$\Delta S_{mix} = -R \sum_{i=1}^{n} x_i \ln x_i \tag{1}$$

Here, x_i is the mole fraction of component I and n is the number of constituent elements. The MT was obtained only in the MEAs and not in the HEAs. The B2 structure was stable at room temperature in the HEAs. The perfect recovery was obtained in the MEAs under larger applied stress compared with the ternary TiPdZr alloys [18]. This is due to the large lattice distortion in the MEAs than the ternary alloys, also known as the multi-component effect.

A previous study showed that although Pt addition effectively increased MTTs because TiPt has MT, extremely high MTT easily introduced plastic deformation in the austenite phase [32, 33]. Then, Co was selected instead of Pt in this study because the B2 structure is stable in TiCo, and Co addition leads to no segregation or precipitation in TiPd. However, it is also expected that Co addition drastically decreases MTTs. Then, understanding of the effect of Co addition on MTT is important to design new HT-SMAs. In this study, through the investigation of TiZrPd (Ni, Co), the effect of single Ni or Co addition and simultaneous addition of Ni and Co to TiZrPd and the multi-component effect on MT and SME was investigated.

Experimental Procedure

18 g ingots with nominal compositions shown in Table 1 were prepared by arc melting in an Ar atmosphere. In this study, Ni or Co was added to replace Pd, while the concentration of Ti and Zr were held at 45 and 5 at.%. In addition to single Ni or Co addition, the simultaneous addition of Ni and Co was performed. For the simultaneous addition, the total concentration of Ni and Co were held at 10 at.% and the ratio of Ni to Co was changed.

The alloy ingots were compressed to approximately 60% of their original height at 1000 °C in the B2 region. The compressed ingots were cut into samples of $5 \times 15 \times 6$ mm. The samples were sealed in silica tubes with argon gas and solution-treated at 1000 °C for 3 h, followed by quenching in iced water.

Samples with $4 \times 4 \times 1$ mm dimensions were cut from the solution-treated samples, embedded in resins, and polished mechanically until the surfaces became mirror planes. Then, the microstructures were observed in backscattered mode by a scanning electron microscope (JEOL 7001F, JEOL) at an accelerating voltage of 20 kV.

Samples for differential scanning calorimetry (DSC, DSC3200s, Material Analysis and Characterization) were prepared by cutting disk-shaped specimens from the solution-treated samples. These specimens had a diameter of 4 mm, a thickness of 1 mm, and weighed approximately 100 mg. MTTs were measured in DSC with heating and cooling rates of 10 °C/min.

Plate-like samples with $10 \times 15 \times 1$ mm dimensions were cut from the solution-treated samples, and the constituent phase was identified by X-ray diffraction (XRD) analysis (RINT-TTR III, Rigaku) using Cu-Kα radiation at 50 kV and 300 mA at room temperature.

Thermal cyclic tests were performed using specimens with $3 \times 3 \times 5$ mm dimensions in the temperature range $M_f - 30$ to $A_f + 30$ °C under compressive stresses (Shimadzu AG–X, Shimadzu) to investigate the shape memory effects of the alloys. In the thermal cyclic test, the sample was first heated to $A_f + 30$ °C, then cooled to $M_f - 30$ °C, and again heated to $A_f + 30$ °C. The sample length was directly measured by a CCD camera. The strain recovery

Table 1 MTT and temperature hysteresis (°C)

Alloy composition (at.%)	A_s	A_f	M_s	M_f	Hysteresis ($A_f - M_s$)
$Ti_{50}Pd_{50}$ [17]	568	587	527	515	72
$Ti_{50}Zr_5Pd_{50}$ [17]	493	509	467	445	42
$Ti_{45}Zr_5Pd_{40}Ni_{10}$	216	258	206	177	52
$Ti_{45}Zr_5Pd_{30}Ni_{20}$	–	–	–	–	–
$Ti_{45}Zr_5Pd_{40}Co_{10}$	303	361	339	298	22
$Ti_{45}Zr_5Pd_{40}Ni_8Co_2$	201	273	212	199	61
$Ti_{45}Zr_5Pd_{40}Ni_5Co_5$	–	–	–	–	–
$Ti_{45}Zr_5Pd_{40}Ni_2Co_8$	143	189	135	108	54

and the work output were estimated using the following equations from the strain-temperature curves:

$$\text{Strain recovery ratio, } r(\%) = \varepsilon_r/\varepsilon_t, \quad (2)$$

$$\text{Work output, } w \left(J/cm^3\right) = \varepsilon_r \times \sigma_a (MPa). \quad (3)$$

Here, ε_r, ε_t, and σ_a represent the recovery strain, the transformation strain, and the applied stress, respectively.

Training, i.e., repeated thermal cyclic testing under constant stress, was also applied to improve the shape recovery and investigate the stability of SME.

Results and Discussion

Microstructure and Constituent Phase

The backscattered electron images of the solution-treated alloys are shown in Fig. 1. A typical multivariant martensite twin structure was observed in $Ti_{45}Zr_5Pd_{40}Ni_{10}$, $Ti_{45}Zr_5Pd_{40}Co_{10}$, $Ti_{45}Zr_5Pd_{40}Ni_8Co_2$, and $Ti_{45}Zr_5Pd_{40}Ni_2Co_8$. On the other hand, the martensite twin structure was not

observed in $Ti_{45}Zr_5Pd_{30}Ni_{20}$ and $Ti_{45}Zr_5Pd_{40}Ni_5Co_5$. The microstructural observations indicate that the MT occurs in $Ti_{45}Zr_5Pd_{40}Ni_{10}$, $Ti_{45}Zr_5Pd_{40}Co_{10}$, $Ti_{45}Zr_5Pd_{40}Ni_8Co_2$, and $Ti_{45}Zr_5Pd_{40}Ni_2Co_8$, but it does not occur in $Ti_{45}Zr_5Pd_{30}Ni_{20}$ and $Ti_{45}Zr_5Pd_{40}Ni_5Co_5$. Ti_2Pd precipitates (a few μm in size) were formed mainly on the grain boundaries and occasionally inside the grains.

The XRD patterns obtained at room temperature are shown in Fig. 2. The B19 structure was clearly identified in $Ti_{45}Zr_5Pd_{40}Ni_{10}$, $Ti_{45}Zr_5Pd_{40}Co_{10}$, $Ti_{45}Zr_5Pd_{40}Ni_8Co_2$, and $Ti_{45}Zr_5Pd_{40}Ni_2Co_8$, but the B2 structure was found in $Ti_{45}Zr_5Pd_{30}Ni_{20}$ and $Ti_{45}Zr_5Pd_{40}Ni_5Co_5$. The results of XRD agrees well with the microstructural observation that the MT occurred in $Ti_{45}Zr_5Pd_{40}Ni_{10}$, $Ti_{45}Zr_5Pd_{40}Co_{10}$, $Ti_{45}Zr_5Pd_{40}Ni_8Co_2$, and $Ti_{45}Zr_5Pd_{40}Ni_2Co_8$, but not in $Ti_{45}Zr_5Pd_{30}Ni_{20}$ and $Ti_{45}Zr_5Pd_{40}Ni_5Co_5$.

MTT

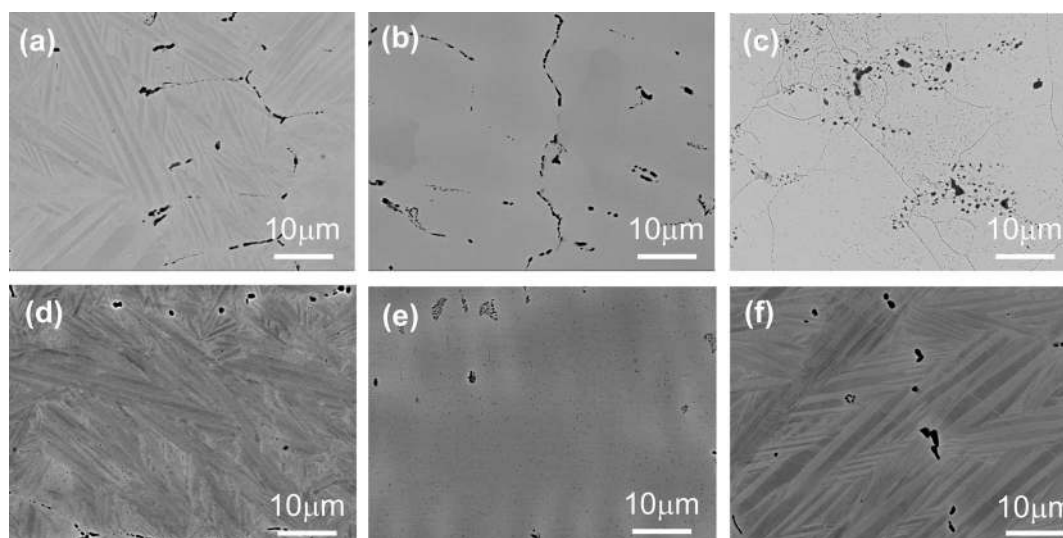The DSC curves of the alloys are shown in Fig. 3. As expected from the microstructural observation and the

Fig. 1 Backscattered electron images of **a** $Ti_{45}Zr_5Pd_{40}Ni_{10}$, **b** $Ti_{45}Zr_5Pd_{30}Ni_{20}$, **c** $Ti_{45}Zr_5Pd_{40}Co_{10}$, **d** $Ti_{45}Zr_5Pd_{40}Ni_8Co_2$, **e** $Ti_{45}Zr_5Pd_{40}Ni_5Co_5$, and **f** $Ti_{45}Zr_5Pd_{40}Ni_2Co_8$
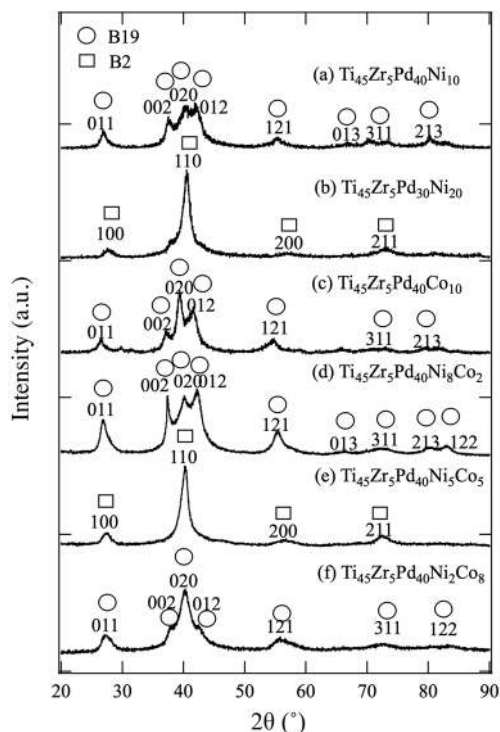
Fig. 2 XRD patterns of **a** $Ti_{45}Zr_5Pd_{40}Ni_{10}$, **b** $Ti_{45}Zr_5Pd_{30}Ni_{20}$, **c** $Ti_{45}Zr_5Pd_{40}Co_{10}$, **d** $Ti_{45}Zr_5Pd_{40}Ni_8Co_2$, **e** $Ti_{45}Zr_5Pd_{40}Ni_5Co_5$, and **f** $Ti_{45}Zr_5Pd_{40}Ni_2Co_8$ at room temperature

XRD analysis, the peaks indicating the MT was observed in $Ti_{45}Zr_5Pd_{40}Ni_{10}$, $Ti_{45}Zr_5Pd_{40}Co_{10}$, $Ti_{45}Zr_5Pd_{40}Ni_8Co_2$, and $Ti_{45}Zr_5Pd_{40}Ni_2Co_8$ but not in $Ti_{45}Zr_5Pd_{30}Ni_{20}$ and $Ti_{45}Zr_5Pd_{40}Ni_5Co_5$. The A_s, A_f, M_s, and martensite finish (M_f) temperatures obtained by DSC are summarized in Table 1 together with the temperature hysteresis between

A_f and M_s. For reference, the MTTs of $Ti_{50}Pd_{50}$ and $Ti_{45}Pd_{50}Zr_5$ [17] are also shown in Table 1. The MTTs are plotted as the functions of Ni and Co concentration in Fig. 4. Compared with $Ti_{45}Pd_{50}Zr_5$, the MTT decreased with the single addition of Ni or Co or the simultaneous addition of Ni and Co. 1 at.% Ni addition decreased A_s by 27 °C, A_f by 25 °C, M_s by 26 °C, and M_f by 27 °C. MTTs by the addition of 20 at.% Ni decreased to lower than 0 °C as the MTTs decreased with the same ratio up to 20 at.%. Then, it is reasonable that no MT was observed in $Ti_{45}Zr_5Pd_{30}Ni_{20}$. On the other hand, 1 at.% Co addition decreased A_s by 19 °C, A_f by 15 °C, M_s by 13 °C, and M_f by 15 °C. The decreases in MTTs by Co addition were smaller than those by the addition of Ni. This is not expected since no MT takes place in TiCo, and the B2 structure is much more stable in TiCo than in TiNi. It is expected that Co addition decreases MTTs more than Ni addition, but the opposite trend occurs in the multi-component alloys. Interestingly, the MTTs of the alloy with 8 Ni and 2 Co were higher than those of the alloy with 2 Ni and 8 Co. Moreover, no MT was observed in $Ti_{45}Zr_5Pd_{40}Ni_5Co_5$. Since the total addition of Ni and Co were 10 at.% for $Ti_{45}Zr_5Pd_{40}Ni_8Co_2$, $Ti_{45}Zr_5Pd_{40}Ni_5Co_5$, and $Ti_{45}Zr_5Pd_{40}Ni_2Co_8$, it is considered that the MTTs of $Ti_{45}Zr_5Pd_{40}Ni_5Co_5$ are between those of $Ti_{45}Zr_5Pd_{40}Ni_8Co_2$ and $Ti_{45}Zr_5Pd_{40}Ni_2Co_8$. However, the B2 structure was stable at room temperature, and the MT was not observed in $Ti_{45}Zr_5Pd_{40}Ni_5Co_5$. The mixing entropy effect is similar to HEAs when the amount of the alloying element is equivalent. In the case of $Ti_{45}Zr_5Pd_{40}Ni_5Co_5$, the amount of Zr, Ni, and Co were 5 at.%, and the mixing entropy shown in Eq. (1) was slightly higher, 1.18R than
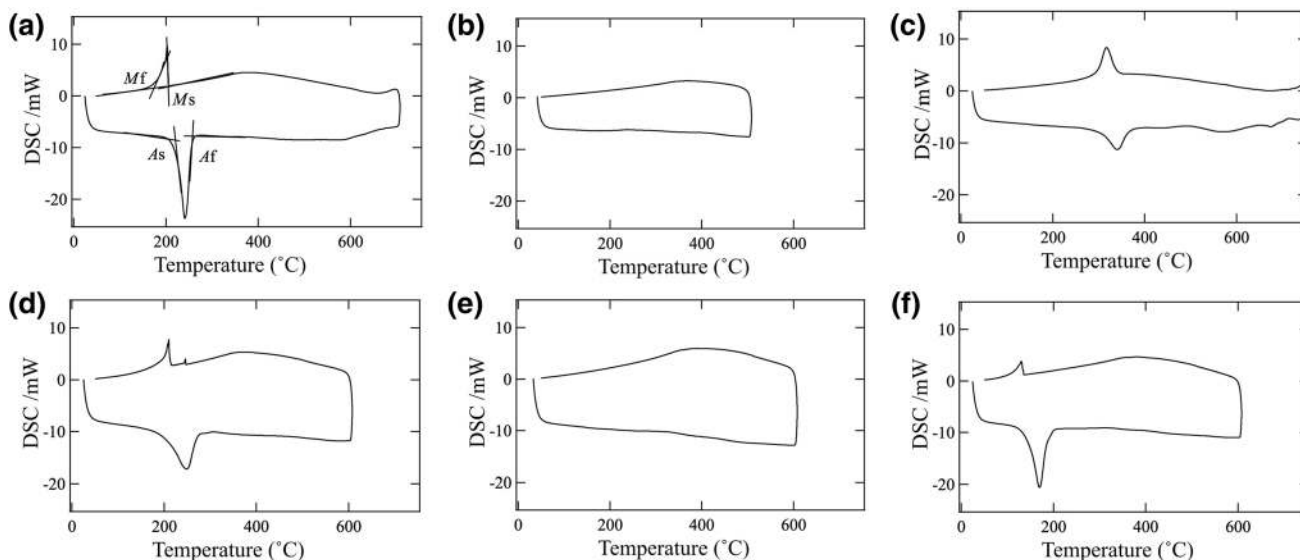

Fig. 3 DSC curves of **a** $Ti_{45}Zr_5Pd_{40}Ni_{10}$, **b** $Ti_{45}Zr_5Pd_{30}Ni_{20}$, **c** $Ti_{45}Zr_5Pd_{40}Co_{10}$, **d** $Ti_{45}Zr_5Pd_{40}Ni_8Co_2$, **e** $Ti_{45}Zr_5Pd_{40}Ni_5Co_5$, and **f** $Ti_{45}Zr_5Pd_{40}Ni_2Co_8$
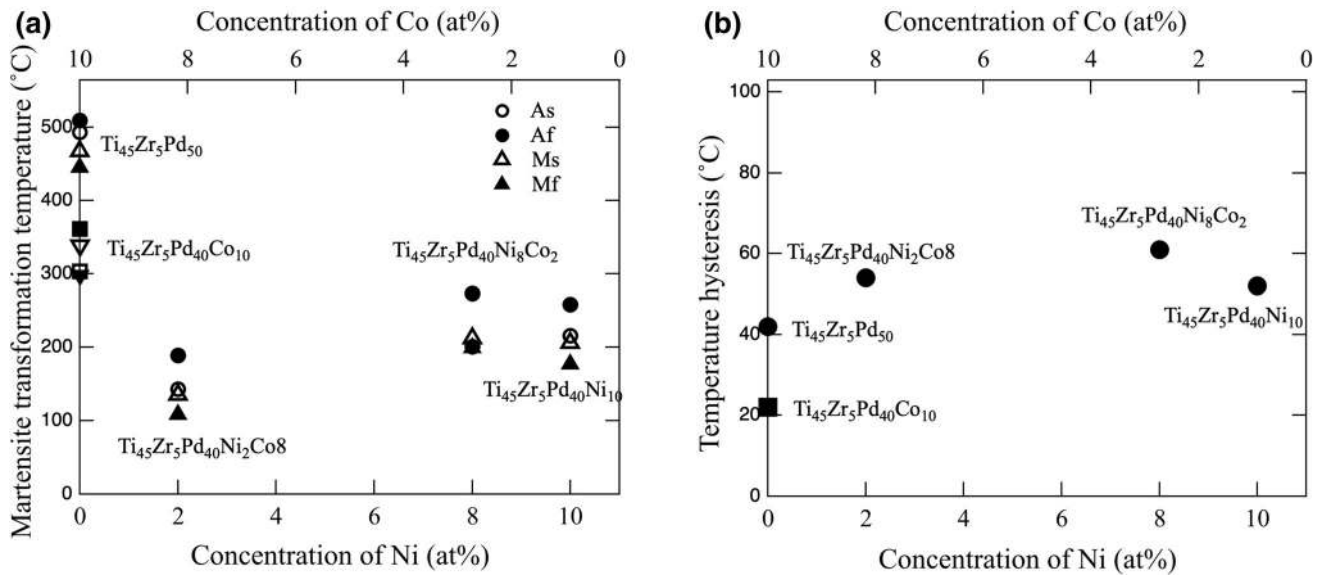
Fig. 4 MTT and temperature hysteresis of tested alloys together with $Ti_{45}Zr_5Pd_{50}$ [17] as a function of Ni and Co concentration. Martensite start (M_s), martensite finish (M_f), austenite start (A_s), and austenite finish (A_f) temperatures are shown

other multi-component alloys, 1.16R. In HEA, for example, the MT occurred, and the B19 structure appeared at room temperature in $Ti_{16.667}Zr_{16.667}Hf_{16.667}Co_{25}Ni_{25}$ with a mixing entropy of 1.23R. On the other hand, no MT was found, and the B2 structure appeared at room temperature in $Ti_{16.667}Zr_{16.667}Hf_{16.667}Co_{16.667}Ni_{16.667}Cu_{16.667}$ with equiatomic composition and the mixing entropy of 1.47R [11]. The equivalent addition of the alloying elements causes partially large lattice distortion and restrains MT, as observed in partially equivalent TiPdZrV [18]. The MTTs of $Ti_{45}Pd_{50}Zr_5$ and $Ti_{45}Pd_{50}V_5$ were approximately 450 °C. The simultaneous addition of Zr and V while keeping the total composition at 5 at.%, decreased M_s and M_f. M_s and M_f were the lowest in $Ti_{45}Pd_{50}Zr_{2.5}V_{2.5}$ with the equivalent amount of Zr and V and the slightly higher mixing entropy of 0.89 R compared with $Ti_{45}Pd_{50}Zr_4V_1$ and $Ti_{45}Pd_{50}Zr_1V_4$ with a mixing entropy of 0.88 R. In TiZrPdNiPt, the B2 structure was stable, and no MT was found in HEAs, such as $Ti_{35}Zr_{15}Pd_{20}Ni_{15}Pt_{15}$ and Ti_{40}-$Zr_{10}Pd_{20}Ni_{15}Pt_{15}$ with the mixing entropy of 1.5R [34]. On the other hand, in the MEA with the smaller mixing entropy of 1.3R and 1.4R than HEA, $Ti_{45}Zr_5Pd_{20}Ni_5Pt_{25}$ and $Ti_{45}Zr_5Pd_{20}Ni_{10}Pt_{20}$, the MT was observed. Although the absolute value of the mixing entropy does not indicate the trend of MTTs in general, when comparing across the same combinations of alloying elements, a higher mixing entropy indicates that MTs are less likely.

The temperature hysteresis between A_f and M_s of the tested alloys were all between 40 °C and 61 °C, which is acceptable for actuators. As shown in Fig. 4, the temperature hysteresis of TiPdZrNiCo was larger than those of TiZrPdNi and TiZrPdCo. Generally, high-entropy SMAs

have a larger temperature hysteresis than conventional SMAs because the severe lattice distortion restrains MT and reverse MT. High-entropy SMAs have lower M_s and higher A_s than those of conventional SMAs [11–14]. In our case, we believe that slightly higher mixing entropy caused larger lattice distortions and the MT became more difficult, resulting in large temperature hysteresis.

SME

The strain-temperature curves based on thermal cyclic testing are shown in Fig. 5. The applied stress ranged from 15 to 200 MPa. In $Ti_{45}Zr_5Pd_{40}Ni_{10}$, the perfect strain recovery was obtained for up to 50 MPa, and a small irrecoverable strain was observed over 100 MPa, as shown in Fig. 5a. A similar behavior was observed in multi-component alloys, $Ti_{45}Zr_5Pd_{40}Ni_8Co_2$, and $Ti_{45}Zr_5Pd_{40}$-Ni_2Co_8, shown in Fig. 5c, d. However, a significant difference compared with $Ti_{45}Zr_5Pd_{40}Ni_{10}$ is that the extra cooling was necessary to return to the original position during cooling, as shown by the arrows. It means that the actual temperature hysteresis of the multi-component alloys was over 100 °C. In $Ti_{45}Zr_5Pd_{40}Co_{10}$, the transformation strain was much smaller, < 1% compared with the other three alloys, and the perfect strain recovery was obtained for up to 200 MPa.

The transformation, the recoverable and irrecoverable strains were estimated from the strain-temperature curves in Fig. 5 and plotted, as shown in Fig. 6a, b. The transformation strains of $Ti_{45}Zr_5Pd_{40}Ni_{10}$, $Ti_{45}Zr_5Pd_{40}Ni_8Co_2$, and $Ti_{45}Zr_5Pd_{40}Ni_2Co_8$ at 200 MPa were between 3.5 and 6%. On the other hand, the transformation strain of
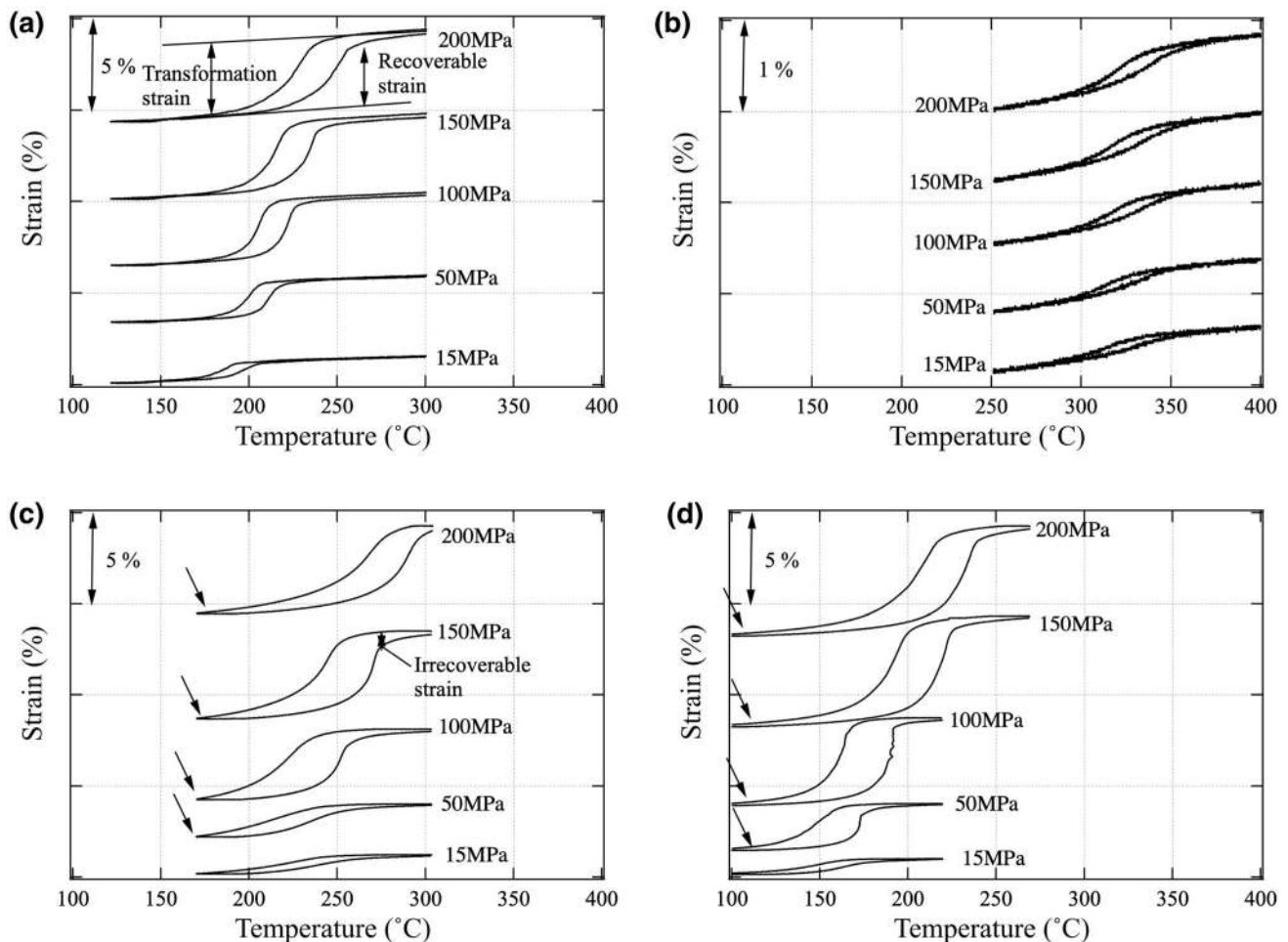
Fig. 5 Strain-temperature curves of thermal cycle test between 15 and 200 MPa for **a** $Ti_{45}Zr_5Pd_{40}Ni_{10}$, **b** $Ti_{45}Zr_5Pd_{40}Co_{10}$, **c** $Ti_{45}Zr_5Pd_{40}Ni_8Co_2$, and **d** $Ti_{45}Zr_5Pd_{40}Ni_2Co_8$

$Ti_{45}Zr_5Pd_{40}Co_{10}$ was approximately 0.5% at 200 MPa in Fig. 6a. This indicates that Co reduced the unit cell volume difference between martensite and austenite. In the previous study, the transformation strain was approximately 5% for $Ti_{45}Zr_5Pd_{50}$ [33], 4.5% for $Ti_{45}Zr_5Pd_{45}Pt_5$ [33], 3% for $Ti_{45}Zr_5Pd_{25}Pt_5$ [33], 2% for $Ti_{45}Zr_4V_1Pd_{50}$ [18], and 3% for $Ti_{45}Zr_5Pd_{20}Ni_5Pt_{25}$ [34]. Expect for $Ti_{45}Zr_5Pd_{40}Co_{10}$, the alloys in the present study have relatively large transformation strain. The transformation strains of $Ti_{45}Zr_5Pd_{40}Ni_8Co_2$, and $Ti_{45}Zr_5Pd_{40}Ni_2Co_8$ were larger than that of $Ti_{45}Zr_5Pd_{40}Ni_{10}$, indicating the effect of multi-component alloying. However, the highest three transformation strains were obtained in the alloy with 8 at.% Co, 2 at.% Co, and 0 at.% Co, respectively, even though the smallest transformation strain was obtained in $Ti_{45}Zr_5Pd_{40}Co_{10}$ with 10 at.% Co. The reason is not clear. The respective order of the recoverable strain was the same as the transformation strain, as shown in Fig. 6b. The irrecoverable strains of all the tested alloys were smaller than 0.5% for up to 200 MPa, and the irrecoverable strain was 0 in

$Ti_{45}Zr_5Pd_{40}Co_{10}$. They were smaller than those of other TiPd alloys, which range approximately 1–2% [18, 33, 34]. Then, the strain recovery was 100% for $Ti_{45}Zr_5Pd_{40}Co_{10}$ and over 80% for the other three alloys, as shown in Fig. 6c. The work outputs of the tested alloys, expect for $Ti_{45}Zr_5Pd_{40}Co_{10}$, were between 6 and 10 J/cm^3 at 200 MPa, as shown in Fig. 6d. They are comparable with the work output of $Ti_{45}Zr_5Pd_{50}$ [33] and larger than those of TiZrPdPt [33], TiZrVPd [18], and TiZrPdNiPt [34].

Training Effect

Since the irrecoverable strain was obtained, training, that is, the repeated thermal cyclic tests under constant stress, was performed for $Ti_{45}Zr_5Pd_{40}Ni_{10}$ and $Ti_{45}Zr_5Pd_{40}Co_{10}$ to improve SME and investigate their stability. The strain-temperature curves of $Ti_{45}Zr_5Pd_{40}Ni_{10}$ for 100 cycles under 300 MPa are shown in Fig. 7a. The initial transformation strain was around 5.6%, and the irrecoverable strain was demonstrated for the first cycle. Figure 7b indicates
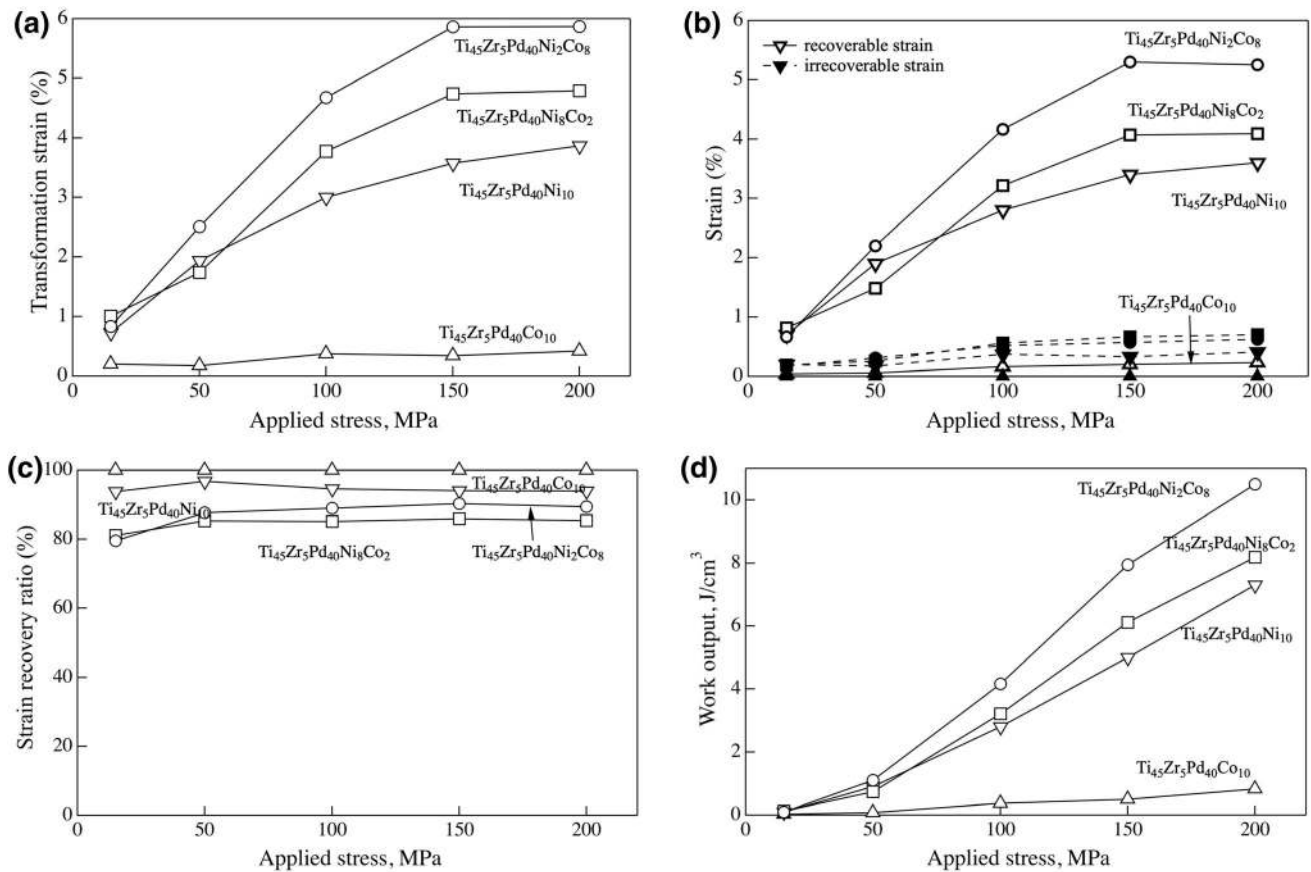
Fig. 6 **a** Transformation strain, **b** recoverable and irrecoverable strain, **c** strain recovery ratio, and **d** work output of $Ti_{45}Zr_5Pd_{40}Ni_{10}$, $Ti_{45}Zr_5Pd_{40}Co_{10}$, $Ti_{45}Zr_5Pd_{40}Ni_8Co_2$, and $Ti_{45}Zr_5Pd_{40}Ni_2Co_8$

the strain-temperature curves of the first nine cycles during which the irrecoverable strain decreased. The perfect recovery was achieved after 20 cycles. The strain-temperature curves of the last nine cycles and comparison of the first and the last nine cycles are shown in Fig. 7c, d, respectively. The nine strain-temperature curves, these traces align almost exactly in Fig. 7c. This indicates that the stable, perfect recovery was obtained under 300 MPa, although the transformation strain became smaller, 3.6%. The work output for the perfect recovery in the last nine cycles was evaluated as 10.8 J/cm³. The shape of the strain-temperature curves of the first cycle and the last nine cycles was drastically changed, as shown in Fig. 7d, that is, A_s and A_f did not change during the thermal cyclic test, but M_s and M_f increased during the thermal cyclic test. Temperature hysteresis became smaller in the last nine cycles compared with the first cycle, as shown in Fig. 7d. The obtained MTTs are summarized in Table 2.

The training was performed under 700 MPa for $Ti_{45}Zr_5Pd_{40}Co_{10}$, and the strain-temperature curves for nine cycles are shown in Fig. 8a. The irrecoverable strain was observed for the first curve, as shown in Fig. 8b, but it disappeared after five cycles. As shown in Fig. 8c, the

work output was approximately 7 J/cm³ for the 9th cycle. In the case of $Ti_{45}Zr_5Pd_{40}Co_{10}$, MTT was approximately constant during the thermal cyclic test, as shown in Fig. 8a and Table 2. However, the decrease in the transformation strain was observed in Fig. 8 that is; 1.3% for the first cycle and 1% for the 9th cycle.

The irrecoverable strain is introduced in two ways during the thermal cyclic test. The first is via the plastic deformation of the austenite phase when the temperature reaches above A_f. The second is via the dislocations formed on the habit plane between the austenite and martensite phases due to the volume difference between the austenite and martensite phases during the thermal cyclic test [35]. In this case, the irrecoverable strain decreases and becomes finally negligible during the repeated thermal cyclic tests because the accumulation of dislocations introduced during phase transformation reduces the number of newly introduced dislocations. For example, the irrecoverable strain disappeared, and the perfect recovery was obtained after 100 cycles in NiTi alloys [35, 36]. The perfect recovery was finally obtained for both $Ti_{45}Zr_5Pd_{40}Ni_{10}$ and $Ti_{45}Zr_5Pd_{40}Co_{10}$, indicating that the irrecoverable strain was
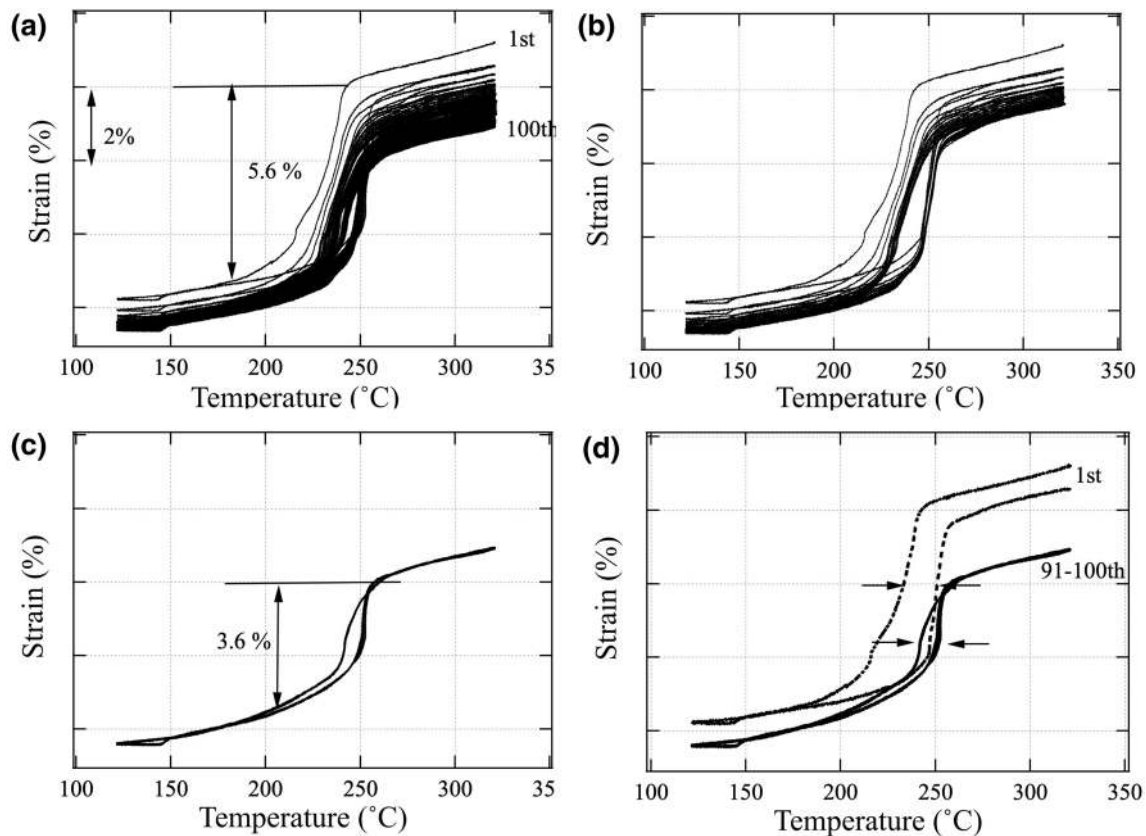
Fig. 7 Strain-temperature curves of $Ti_{45}Zr_5Pd_{40}Ni_{10}$ under 300 MPa. **a** 100 cycles, **b** initial 9 cycles, **c** last 9 cycles and **d** comparison with the 1st cycle and last 9 cycles

Table 2 Comparison of martensitic transformation temperatures obtained by DSC after the TC test (°C)

Alloy composition (at.%)	Method	A_s	A_f	M_s	M_f	Hysteresis ($A_f - M_s$)
$Ti_{45}Zr_5Pd_{40}Ni_{10}$	DSC	216	258	206	177	52
	TC-1st cycle	242	260	244	211	16
	TC-100th cycle	250	260	250	238	10
$Ti_{45}Zr_5Pd_{40}Co_{10}$	DSC	303	361	339	298	22
	TC-1st cycle	294	361	349	280	12
	TC-9th cycle	289	347	340	279	7

introduced by the phase transformation, not the plastic deformation of the austenite phase.

In both alloys, the transformation strain decreased during the thermal cyclic tests, as shown in Figs. 7 and 8. Dislocations were introduced by phase transformation and accumulated on the habit plane. The accumulated dislocations decreased the area of the martensite phase during the repeated thermal cyclic test, and as a result, the total transformation strain decreased. It is likely that the number of accumulated dislocations is less in the alloy with the small transformation strain, that is, the volume difference between the austenite and martensite phases. It is also known that MTTs are affected by applied stress during thermal cyclic testing and increase under large applied

stress. It is considered that the alloy with the large transformation strain needs thermal energy more than the alloy with the small transformation strain for reverse transformation. Then, MTTs will be increased for the alloy with the large transformation strain, but MTTs are not drastically changed for the alloy with the small transformation strain. This is the reason why MTTs became higher in $Ti_{45}Zr_5Pd_{40}Ni_{10,}$ and MTTs were insensitive to doping in $Ti_{45}Zr_5Pd_{40}Co_{10}$ under the applied stress.

The work outputs of the alloys with perfect recovery are plotted in Fig. 9 as a function of A_s together with the previous results [5, 6, 18, 34]. It is clear that the work output drastically decreased with the increase in A_s. The work output of the conventionally used TiNi was between
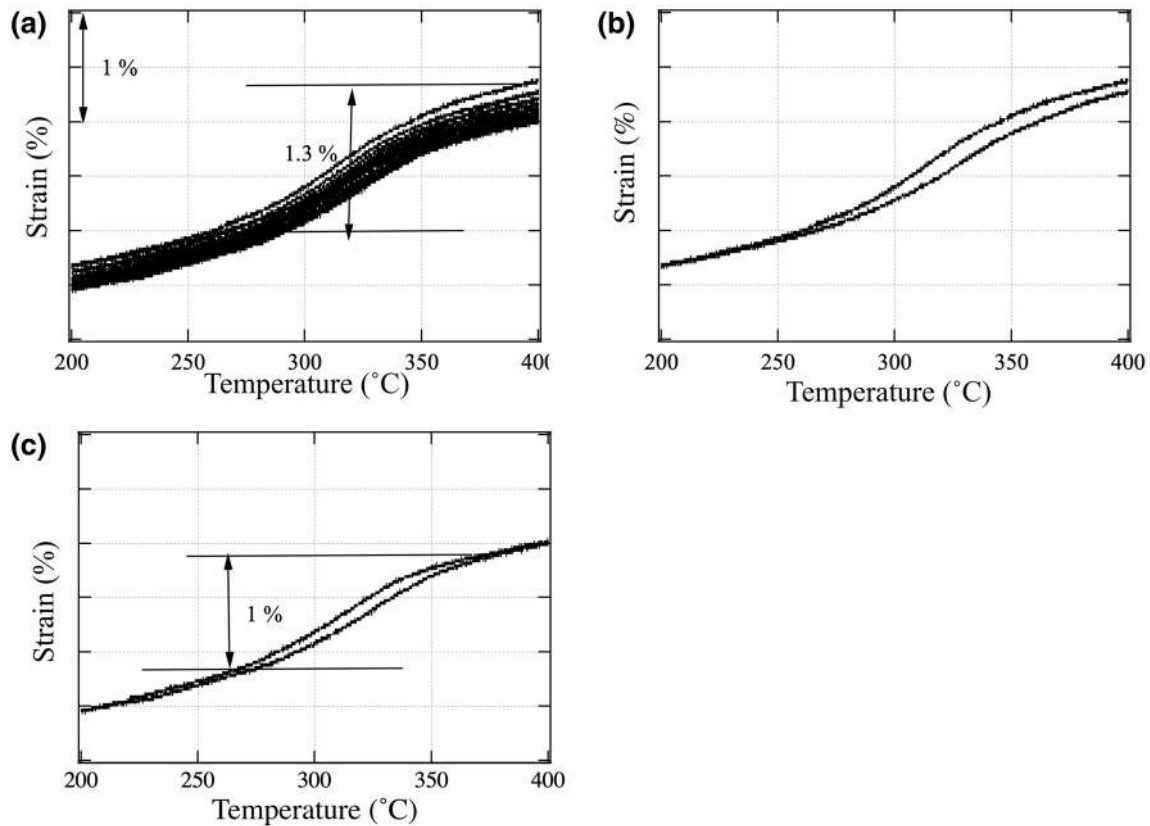
Fig. 8 Strain-temperature curves of $Ti_{45}Zr_5Pd_{40}Co_{10}$ under 700 MPa. a 9 cycles, b the 1st cycle, and c the 9th cycle
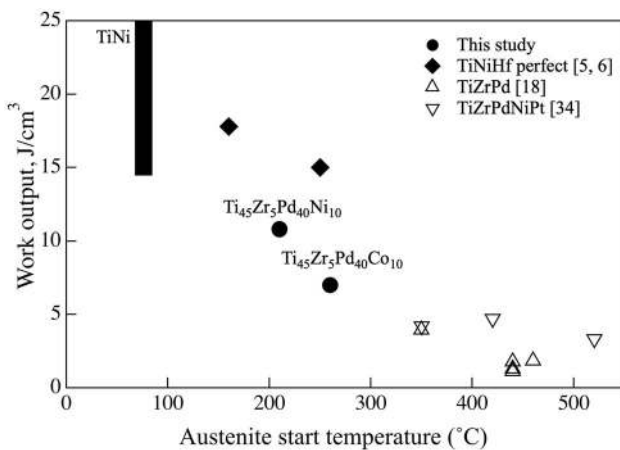
Fig. 9 Comparison of the work output as a function of A_s

Conclusions

The effects of the addition of Ni and/or Co to $Ti_{45}Zr_5Pd_x$ on phase transformation and strain recovery were investigated. The MT occurred in $Ti_{45}Zr_5Pd_{40}Ni_{10}$, $Ti_{45}Zr_5Pd_{40}Co_{10}$, $Ti_{45}Zr_5Pd_{40}Ni_8Co_2$, and $Ti_{45}Zr_5Pd_{40}Ni_2Co_8$. However, in $Ti_{45}Zr_5Pd_{30}Ni_{20}$ and $Ti_{45}Zr_5Pd_{40}Ni_5Co_5$, the MT did not occur and B2 structure remained at room temperature. The MTT decreased by the addition of Ni and/or Co. $Ti_{45}Zr_5Pd_{40}Co_{10}$ had the highest MTTs among the tested alloys: A_s, A_f, M_s, and M_f were 303, 361, 339, and 298 °C, respectively. $Ti_{45}Zr_5Pd_{40}Ni_2Co_8$ had the lowest MTTs: A_s, A_f, M_s, and M_f were 143, 189, 135, and 108 °C, respectively. In $Ti_{45}Zr_5Pd_{30}Ni_{20}$, an addition of 1 at.% Ni caused an MTT decrease of approximately 25 °C and the addition of 20 at.% Ni decreased A_f to a temperature lower than 0 °C. In $Ti_{45}Zr_5Pd_{40}Ni_5Co_5$, the relatively large mixing entropy drastically decreased M_s, and the austenite phase becomes stable at room temperature.

The strain recovery was investigated using a thermal cyclic test at 15, 50, 100, 150, and 200 MPa. The perfect recovery was obtained up to 200 MPa in $Ti_{45}Zr_5Pd_{40}Co_{10}$, although the recovery strain was only ∼ 0.4% at 200 MPa. In the other three alloys, $Ti_{45}Zr_5Pd_{40}Ni_{10}$, $Ti_{45}Zr_5Pd_{40}Ni_8Co_2$, and $Ti_{45}Zr_5Pd_{40}Ni_2Co_8$, the small

15 and 25 J/cm³. TiNi-Hf nanoprecipitates indicate almost the same work output as TiNi [5, 6]. In our study, although A_s of $Ti_{45}Zr_5Pd_{40}Co_{10}$ was 303 °C and the perfect recovery was obtained, the work output was minimal due to the small recovery of strain. $Ti_{45}Zr_5Pd_{40}Co_{10}$ indicated stability under 700 MPa, but A_s were lower to 260 °C. As a result, the advantage as HT-SMA was not obtained. MTTs of the other alloys were ∼ 200 °C. Therefore, Ni and/or Co addition to TiPd is not suitable to obtain HT-SMAs.

irrecoverable strain was found. However, the repeated thermal cyclic test decreased the irrecoverable strain, until the perfect strain recovery was obtained. The stabilized cycles with perfect recovery were obtained under 300 MPa in $Ti_{45}Zr_5Pd_{40}Ni_{10}$. The work output was approximately 10.8 J/cm^3 at an A_s of 210 °C. The perfect recovery was obtained under 700 MPa in $Ti_{45}Zr_5Pd_{40}Co_{10}$. The work output of 7 J/cm^3 was obtained at an A_s of 260 °C.

References

1. Ma J, Karaman I, Noebe RD (2010) High temperature shape memory alloys. Int Mater Rev 55:257–315
2. Bigelow GS, Garg A, Padula SA, Gaydosh DJ, Noebe RD (2011) Load-biased shape-memory and superelastic properties of precipitation strengthened high-temperature Ni50.3Ti29.7Hf20 alloy. Scr. Mater. 64:725–728
3. Coughlin DR, Phillips PJ, Bigelow GS, Garg A, Noebe RD, Mills MJ (2012) Characterization of the microstructure and mechanical properties of a 50.3Ni-29.7Ti-20Hf shape memory alloy. Scr. Mater. 67:112–115
4. Benafan O, Noebe RD, Padula SA, Vaidyanathan R (2012) Microstructural response during isothermal and isobaric loading of a precipitation-strengthened Ni-29.7Ti-20Hf high-temperature shape memory alloy. Metall Mater Trans A 43:4539–4552
5. Karaca HE, Saghaian SM, Ged G, Tobe H, Basaran B, Maier HJ, Noebe RD, Chumlyakov YI (2013) Effects of nanoprecipitation on the shape memory and material properties of an Ni-rich NiTiHf high temperature shape memory alloy. Acta Mater 61:7422–7431
6. Benafan O, Grag A, Noebe RD, Bigelow GS, Padula SA, Gaydosh DJ, Schell N, Mabe JH, Vaidyanathan R (2014) Mechanical and functional behavior of a Ni-rich Ni 50.3 Ti 29.7 Hf 20 high temperature shape memory alloy. Intermet. 50:94–107
7. Shuitcev A, Vasin RN, Fan XM, Balagurov AM, Bobrikov IA, Li L, Golovin IS, Tong YX (2020) Volume effect upon martensitic transformation in $Ti_{29.7}Ni_{50.3}Hf_{20}$ high temperature shape memory alloy. Scr. Mater. 178:67–70
8. Karakoc O, Hayrettin C, Evirgen A, Santamarta R, Canadinc D, Wheeler RW, Wang SJ, Lagoudas DC, Karaman I (2019) Role of microstructure on the actuation fatigue performance of Ni-Rich NiTiHf high temperature shape memory alloys. Acta Mater 175:107–120
9. Hayrettin C, Karakoc O, Karaman I, Mabe JH, Santamarta R, Pons J (2019) Two way shape memory effect in NiTiHf high-temperature shape memory alloy tubes. Acta Mater 163:1–13
10. Umale T, Salas D, Tomes B, Arroyave R, Karaman I (2019) The effects of wide range of compositional changes on the martensitic transformation characteristics of NiTiHf shape memory alloys. Scr Mater 161:78–83
11. Fistov GS, Kosorukova TA, Koval YN, Odnosum VV (2015) High entropy shape memory alloys. Mater Today Proc 2:S499–S503
12. Chen C-H, Chen Y-J (2019) Shape memory characteristics of $(TiZrHf)_{50}Ni_{25}Co_{10}Cu_{15}$ high entropy shape memory alloy. Scr Mater 162:185–189
13. Lee H-C, Chen Y-J, Chen C-H (2019) Effect of solution treatment on the shape memory functions of $(TiZrHf)_{50}Ni_{25}Co_{10}Cu_{15}$ high entropy shape memory alloy. Entropy 21:1027–1041
14. Canadinc D, Trehern W, Ma J, Karaman I, Sun F, Chaudhry Z (2019) Ultra-high temperature multi-component shape memory alloys. Scr Mater 158:82–87
15. Yamabe-Mitarai Y, Arockiakumar R, Wadood A, Suresh KS, Kitashima T, Hara T, Shimojo M, Tasaki W, Takahashi M, Taahashi S, Hosoda H (2015) Ti(Pt, Pd, Au) based high temperature shape memory alloys. Mater Today Proc 2:S517–S522
16. Arockiakumar R, Takahashi M, Takahashi S, Yamabe-Mitarai Y (2013) Microstructure, mechanical, and shape memory properties of Ti-55Pd-5x (x=Zr, Hf, V, Nb) alloys. Mater Sci Eng A 585:86–93
17. Kawakita M, Takahashi M, Takahashi S, Yamabe-Mitarai Y (2012) Effect of Zr on phase transformation and high-temperature shape memory effect in TiPd alloys. Mater Lett 89:336–338
18. Sato H, Kim H-Y, Shimojo M, Yamabe-Mitarai Y (2017) Training effect on microstructure and shape recovery in Ti-Pd-Zr Alloys. Mater Trans 58(10):1479–1486
19. Wadood A, Hosoda H, Yamabe-Mitarai Y (2014) Phase transformation, oxidation, and shape memory properties of Ti-50Au-10Zr alloy for high temperature applications. J Alloys Compd 595:200–205
20. Wadood A, Yamabe-Mitarai Y (2015) Silver- and zirconium-added ternary and quaternary TiAu based high temperature shape memory alloys. J Alloy Compd 646:1172–1177
21. Yamabe-Mitarai Y, Hara T, Miura S, Hosoda H (2006) Mechanical properties of Ti-50(Pt, Ir) high-temperature shape memory alloys. Mat Trans 47(3):650–657
22. Nishida M, Matsuda M, Yasumoto Y, Yano S, Yamabe-Mitarai Y, Hara T (2008) Crystallography and morphology of twins in equiatomic TiPt martensite. Mater Sci Technol 24(8):884–889
23. Yamabe-Mitarai Y, Hara T, Miura S, Hosoda H (2010) Shape memory effect and pseudoelasticity of TiPt. Intermet 18:2275–2280
24. Yamabe-Mitarai Y, Hara T, Miura S, Hosoda H (2012) Phase transformation and shape memory effect of Ti(Pt, Ir). Metall Trans A 43A:2901–2911
25. Wadood A, Takahashi M, Takahashi S, Hosoda H, Yamabe-Mitarai Y (2013) High-temperature mechanical and shape memory properties of TiPt-Zr and TiPt-Ru alloys. Mater Sci Eng A 564:34–41
26. Yamabe-Mitarai Y, Hara T, Kitashima T, Miura S, Hosoda H (2013) Composition dependence of phase transformation behavior and shape memory effect of Ti(Pt, Ir). J Alloys Compd 577S:S399–S403
27. Wadood A, Yamabe-MItarai Y (2014) Recent research developments related to near-equiatomic TiPt alloys for high-temperature (above 800 °C) applications. Platin Met Rev 58(2):61–67
28. Wadood A, Yamabe-Mitarai Y (2014) TiPd-Co and TiPt-Ru high temperature shape memory alloys. Mater Sci Eng A 610:106–110
29. Yamabe-Mitarai Y, Wadood A, Arockiakumar R, Hara T, Takahashi M, Takahashi S, Hosoda H (2014) Phase transformation and shape memory effect of Ti(Pt, Ir). Mater Sci Forum 783–786:2541–2545
30. Donkersloot HC, Van Vucht JHN (1970) Martensitic transformations in gold-titanium, palladium-titanium and platinum-titanium alloys near the equiatomic composition. J Less Common Met 20(2):83–91
31. Villars P, Okamoto H, Cenzual K (eds) (2006) ASM Alloy Phase Diagrams Center https://www1.asminternational.org/AsmEnterprise/APD, ASM International, Materials Park, OH
32. Yamabe-Mitarai Y, Takebe W, Shimojo M (2017) Phase transformation and shape memory effect of Ti-Pd-Pt-Zr high temperature shape memory alloys. Shape Mem Superelast 3(4):381–391

33. Tasaki W, Shimojo M, Yamabe-Mitarai Y (2019) Thermal cyclic properties of TI-Pd-Pt-Zr high-temperature shape memory alloys. Crystals 9:595–611

34. Matsuda H, Sato H, Shimojo M, Yamabe-Mitarai Y (2019) Improvement of high-temperature shape-memory effect by multi-component alloying for TiPd alloys. Mater Trans 60(11):2281–2291

35. Atli KC, Karaman I, Noebe RD, Gaydosh D (2013) The effect of training on two-way shape memory effect of binary NiTi and NiTi based ternary high temperature shape memory alloys. Mater Sci Eng A 560:653–666

36. Atli KC, Franco BE, Karaman I, Gaydosh D, Noebe RD (2013) Influence of crystallographic compatibility on residual strain of TiNi based shape memory alloys during thermo-mechanical cycling. Mater Sci Eng A 574:9–16